Two-body disintegration of the deuteron with 0.8–1.8 GeV photons

S. J. Freedman,* D. F. Geesaman, R. Gilman,† M. C. Green,‡ R. J. Holt,
H. E. Jackson, E. R. Kinney,§ R. Kowalczyk, C. Marchand,‖ J. Napolitano,¶
J. Nelson, D. H. Potterveld, and B. Zeidman
Physics Division, Argonne National Laboratory, Argonne, Illinois 60439

R. E. Segel and T.-Y. Tung **
Northwestern University, Evanston, Illinois 60201

D. Beck,†† G. Boyd, D. Collins, B. W. Filippone, C. E. Jones‡‡ J. Jourdan,§§
R. D. McKeown, R. Milner,‖‖ and R. Walker,¶¶
California Institute of Technology, Pasadena, California 91125

P. E. Bosted
American University, Washington, D.C. 20016

Z.-E. Meziani
Stanford University, Stanford, California 94305

R. Minehart
University of Virginia, Charlottesville, Virginia 22901

(Received 7 May 1993)

The differential cross section for the reaction $^2H(\gamma,p)n$ has been measured at several center-of-mass angles ranging from 50° to 143° for photon energies between 0.8 and 1.8 GeV. The experiment was performed at the SLAC-NPAS facility with the use of the 1.6 GeV/c spectrometer to detect the high energy protons produced by a bremsstrahlung beam directed at a liquid deuterium target. Contributions from concurrent disintegration by the residual electron beam were determined by measuring the proton yield without the Cu photon radiator. At angles not very far from 90°, the energy dependence of the cross sections is consistent with predictions of scaling using counting rules for consitituent quarks. At least one theoretical calculation based on a meson-baryon picture of the reaction is able to reproduce the magnitude and energy dependence of the 90° cross section. The angular distribution exhibits a large enhancement at backward angles at the higher energies.

PACS number(s): 25.20.Lj, 24.85.+p, 12.38.Qk, 25.10.+s

I. INTRODUCTION

Photodisintegration of the deuteron is among the simplest of electromagnetic nuclear reactions. Careful measurements of the differential cross section at low energies have provided stringent tests of the deuteron wave function and hence the nucleon-nucleon (NN) potential. At energies above the pion threshold, one also tests the understanding of the dynamics of large energy and momentum absorption by a nucleon pair. When the photon energy becomes commensurate with the rest mass of the nucleon, one begins to look for phenomena which are best

*Permanent address: Dept. of Physics, University of California, Berkeley, CA 94720.
†Permanent address: Dept. of Physics & Astronomy, Rutgers University, Piscataway, NJ 08855.
‡Permanent address: LeCroy Research Systems, Spring Valley, NY 10977.
§Permanent address: Dept. of Physics, University of Colorado, Boulder, CO 80309.
‖Permanent address: Centre d'Etudes Nucléaire de Saclay, 91191 Gif-sur-Yvette, France.
¶Permanent address: Dept. of Physics, Rensselaer Polytechnic Institute, Troy, NY 12180.
**Present address: Dept. of Physics, The College of William and Mary, Williamsburg, VA 23187.
††Permanent address: Dept. of Physics, University of Illinois, Urbana, IL 61801.
‡‡Present address: Physics Division, Argonne National Laboratory, Argonne, IL 60439.
§§Permanent address: Dept. of Physics, University of Basel, CH-4056 Basel, Switzerland.
‖‖Permanent address: Dept. of Physics, Massachusetts Institute of Technology, Cambridge, MA 02139.
¶¶Present address: KEK National Laboratory for High Energy Physics, Oho, Tsukuba 305, Japan.

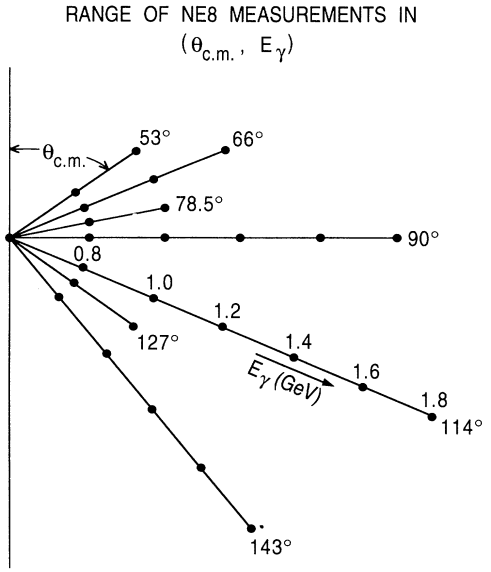

FIG. 1. A depiction of the points in photon energy and center-of-mass angle at which the differential cross section for the photodisintegration reaction was measured in the present experiment.

understood in terms of the nucleon substructure coupled to the NN force.

We report here the results of the first measurement of the differential cross section for the reaction ^{2}H(γ,p)n at photon energies above 1 GeV. The cross sections were measured at several center-of-mass (c.m.) angles ($\theta_{\text{c.m.}}$) in the range 50° to 144°, though not at every photon energy because of the limited beam time available. Figure 1 displays a pictograph of the combinations of photon energy and c.m. angles explored. Preliminary results at 90° in the c.m. have been reported earlier [1].

We expect that these data will provide an important test for calculations based on models of the reaction that use mesons and baryons as fundamental constituents, particularly in the so-called "resonance" region of photonucleon reactions. While calculations based on quark-gluon states and their interactions appear impractical at present, some predictions of the energy dependence or scaling of the differential cross section at fixed c.m. angle have been made and can also be tested. In the latter case, it is of particular interest to know at which energies such scaling may begin, since many expect scaling to occur inevitably at sufficiently high incident energy.

Section II reviews the various theoretical models of the two-body deuteron photodisintegration reaction. In Sec. III the experimental apparatus and method is described, and is followed by the description of the data analysis in Sec. IV. The results are presented in Sec. V and are compared with the available theoretical predictions. Section VI summarizes our conclusions.

II. THEORETICAL BACKGROUND

Interest in simple photonuclear reactions in this energy region has been sparked by the apparent success of perturbative quantum chromodynamics (QCD) in describing exclusive reactions. In particular these calculations accurately predict the energy or momentum transfer dependence of the measured cross sections for elastic electron scattering [2] and meson photoproduction from nucleons [3] at energies not much larger than the nucleon mass. In their simplest form, these predictions are based on counting the minimum number of fundamental pointlike constituents in the reaction, each of which contributes a factor into the amplitude. At energies high relative to the mass of the constituents, several theoretical studies [4, 5] show that at fixed center-of-mass (c.m.) scattering angle the invariant cross section $d\sigma/dt$ for a two-body reaction $AB \to CD$ should scale as the total invariant energy squared s to the power $2-(n_A+n_B+n_C+n_D)$ where n_A is the number of fundamental constituents in particle A, and similarly for B, C, and D. Since this argument is essentially dimensional, it is expected to eventually hold true at some energy. In the cases of pion photoproduction and proton-proton elastic scattering, the scaling limit is apparently reached at energies only a few times the mass of the hadrons involved. For deuteron photodisintegration, one expects an s dependence of s^{-11}. As we have reported elsewhere [1], the energy dependence of the 90° cross section does appear to approach this scaling behavior at energies only slightly above 1 GeV. Indeed, Holt [6] has argued that photoproduction reactions may "scale" at relatively low energies because the momentum transferred to the constituent hadrons is much larger than in electron scattering with the same beam energy.

A variation of this scaling model is reported by Brodsky and Hiller [7] who seek to find the scaling behavior at lower energy by dividing out the form factors of the nucleons, and recalculating the constituent scaling laws treating nucleons as fundamental particles. Their approach is based on a similar treatment of elastic ed scattering [8]. They represent this new measure as the square of a "reduced nuclear amplitude" $f^2(\theta_{\text{c.m.}})$, related to the differential cross section by

$$\frac{d\sigma}{d\Omega_{\text{c.m.}}} = \frac{1}{[s(s-M_d^2)]^{1/2}} F_p^2(\hat{t}_p) F_n^2(\hat{t}_n) \frac{1}{p_T^2} f^2(\theta_{\text{c.m.}}),$$

where

$$\hat{t}_i = (p_i - \tfrac{1}{2}p_d)^2.$$

The nucleon elastic form factors F_p and F_n are written as $F_N(t) = 1/[1 - t/(0.71\ \text{GeV})^2]^2$ which approximates their energy dependence, while M_d is the deuteron mass, and p_T is the nucleon transverse momentum. Neither of these models attempts to describe the magnitude of the cross section, which requires a proper treatment of the quark wave function of the nucleon. It should be noted, however, that some claim that the required normalization is far underestimated in a treatment consistent with perturbative QCD [9].

The most generally successful model used to describe nuclear processes involving relatively low energies and momentum transfers is based on nucleons that interact by exchanging π mesons. Refinements [10] of the model

allow for the transition of the proton or neutron to excited states such as the Δ and the inclusion of other mesons such as ρ, ω, and η. Some calculations also include multiple-pion exchange in terms of the σ, which accounts for the strong s-wave $\pi\pi$ interaction. Calculations [11] based on this model have been applied to the deuteron photodisintegration with only limited success. The best agreement occurs at photon energies below pion threshold where the intermediate mesonic and isobaric states are entirely virtual. Figure 2 indicates the predominant processes in the reaction. Only Laget [12] has extended his predictions from low photon energy to above 500 MeV.

Several theoretical attempts have been made to predict the cross section at photon energies above 1 GeV using the meson-baryon picture. Lee [13] has calculated the photodisintegration cross sections with a dynamical model based on photomeson production followed by meson absorption and final state interactions (FSI). In this model, the photomeson production amplitude is constrained by existing meson production data on the nucleon. The final state interactions are calculated from a nucleon-nucleon model [14] in which π, ρ, Δ, and Roper(1440) degrees of freedom are explicitly included.

Kang *et al.* [15] have used a more complicated and extended model than Lee for the photonucleon coupling, taking into account the effects of all baryon resonances with a mass below 2 GeV and $J \leq \frac{5}{2}$. Meson-exchange effects were modeled using single exchange of π, ρ, and η. Furthermore they claim to have properly included the relativistic structure of the d-NN vertex and maintained gauge invariance in the reaction amplitude. Phenomenological form factors have been used to describe the meson-baryon vertices which have been varied in order to describe the disintegration cross sections at 90°.

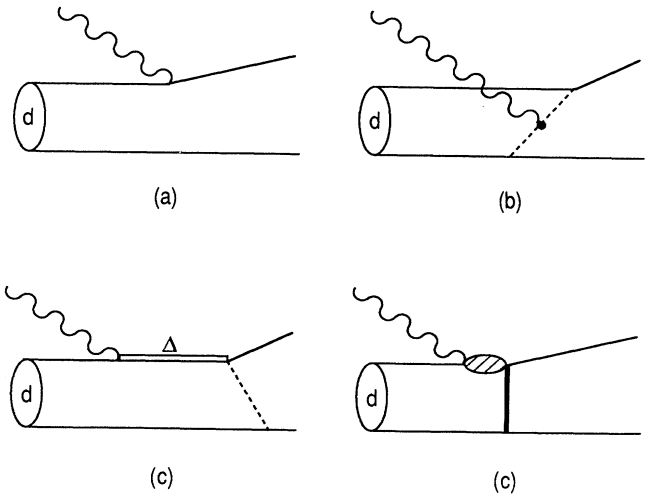

FIG. 2. Diagrams of the major processes contributing to photodisintegration. The Born term is represented in (a) while (b) indicates a typical meson-exchange contribution, (c) shows the mechanism of isobar excitation followed by meson exchange, whereas (d) shows a more general diagram where the crosshatched areas denote complex interactions.

The use of a Hulthèn potential for the deuteron wave function and of monopole form factors with mass parameters that had to be substantially changed as a function of energy make it difficult to assess the relative importance of including the additional baryon resonances.

Finally, a calculation by Nagornyĭ *et al.* [16] uses a much simpler theory based on the vector coupling of the photon to nucleons only, though with form factors for the photon-nucleon vertices and a relativistic model of the deuteron wave function [17]. The effects of the mesons are included implicitly in the momentum-transfer dependence of the form factors, rather than explicitly as in the other calculations. They also include a contact term to guarantee gauge invariance, and their model contains the excitation of the Roper(1440) nucleon resonance as well as its existence as a component of the deuteron wave function.

These theoretical calculations will be compared to the new data in Sec. V.

III. EXPERIMENTAL APPARATUS AND METHOD

The experimental apparatus was located in end station A of the Stanford Linear Accelerator Center (SLAC), and used the intense electron beam produced by the Nuclear Physics Injector [18] to create an intense photon beam. Both electrons and photons impinged upon a liquid deuterium target and outgoing protons were detected in a magnetic spectrometer, as shown schematically in Fig. 3. A plan of the experimental arrangement is shown in Fig. 4. The photon beam was generated via bremsstrahlung of the electron beam in a thin Cu radiator 1 m upstream of the deuterium target. Protons from the two-body disintegration of the deuteron may be unambiguously identified in the momentum range corresponding to incident photons with energies of the end point of the bremsstrahlung spectrum, i.e., the electron beam energy, down to the pion creation threshold. The close proximity of the Cu radiator to the target guarantees that the entire photon flux as well as the residual electron beam intercepts the target. In order to determine the cross sections for reactions induced solely by real photons, the electrodisintegration yield is measured by removing the Cu radiator, and subsequently subtracted from the yield obtained with the Cu radiator in place.

A. Photon beam

The Nuclear Physics Injector uses the last six sectors of the SLAC linac to produce a high intensity electron beam

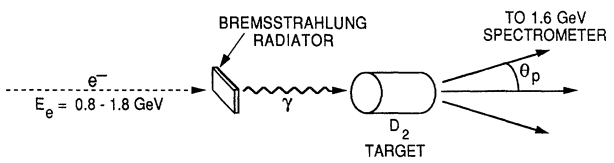

FIG. 3. Schematic of the experimental technique.

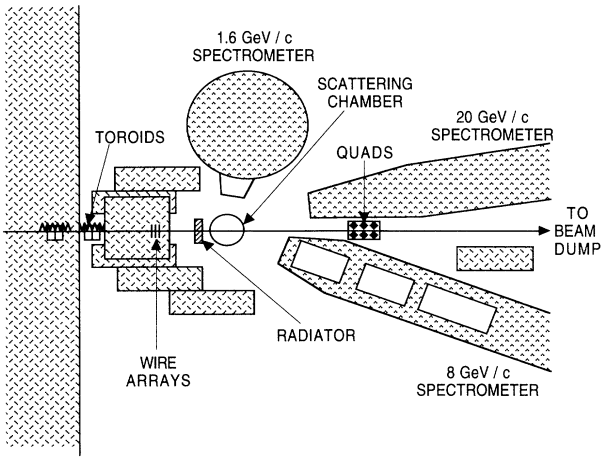

FIG. 4. Plan view of the experimental setup in SLAC end station A.

with energies between 0.5 and 6 GeV, in pulses approximately 1.6 μs long. Typically, the present experiment received pulses with a peak current of up to 20 mA, delivered with a frequency of 80–100 Hz. The beam energy is determined from periodic field measurements with a flip coil in the central field region of a magnet connected in series with those which transport the beam into the end station. The accuracy of this technique is typically 0.1%. The spread in energy of the beam is limited by collimating slits and was typically no more than 0.4%. The current was monitored independently by two nonintercepting toroidal transformers located just upstream of the radiator. These toroids integrated the beam current on a pulse-by-pulse basis and were calibrated every several hours by passing a standard pulse through a tertiary winding of the toroid. Their accuracy is estimated to be 0.2%. After passing through the radiator and target the residual beam was refocused by a quadrupole doublet to minimize room background and directed into a water cooled dump approximately 110 m downstream.

Copper foils of thicknesses 0.255, 0.531, and 0.774 $\pm$ 0.002 g/cm^2, corresponding to approximately 2%, 4%, and 6% radiation lengths, were used to generate bremsstrahlung radiation. At these electron energies, the angular divergence of the photon beam is dominated by the effect of small-angle multiple scattering of the incident electrons, estimated to give a divergence of 5 mrad in the worst case. The radiator location was therefore chosen as close to the deuterium target as possible to ensure that the entire bremsstrahlung cone was intercepted, but without the reaction products from the Cu coming into the acceptance of the spectrometer. This gave a larger count rate than if a collimated beam had been used, which also would have required an independent measurement of the photon flux per incident electron. The flux per electron per unit photon energy was calculated using the Bethe-Heitler extreme relativistic theory with intermediate screening and Coulomb correction for the electron-nucleus radiation added to the electron-electron bremsstrahlung, as implemented in the codes of Matthews and Owens [19]. These calculations also include the effects of the finite energy width of the incident beam as well as ionization and radiative energy loss in the Cu foil [20]. In order to test our understanding of the photon beam, a series of measurements of the proton yield using each of the Cu foils was performed and the results are presented in Fig. 5. The linearity of the yield normalized by the integrated electron current confirms that the entire photon beam is intercepted by the target and that the photon intensity is proportional to the measured beam current. The accuracy of the absolute normalization of the calculations themselves is estimated to be better than 3% at photon energies away from the end-point region.

B. Targets

The target assembly, shown in Fig. 6, consisted of two sets of targets, which were individually moved into the beamline by a combination of rotation and vertical displacement. The cryogenic targets consisted of three pairs of 5 cm diameter flasks, each pair comprising nominal 4 cm and 15 cm long flasks filled with liquid deuterium, liquid hydrogen, and vacuum, respectively. Comparison of the yields from the short and long cells placed a limit on the effect of multiple-step processes in the target.

We used seven additional targets, all thin 0.33 g/cm^2 carbon slabs. One was located at the center target position, and the others were displaced along the beam at $\pm$5.0, $\pm$7.5, and $\pm$10.0 cm. These targets were used for calibration purposes as well as to study the acceptance of the spectrometer as a function of position. This functional dependence is especially important given the extension of the cryogenic targets. Inelastic quasifree electron scattering from protons in carbon was the primary

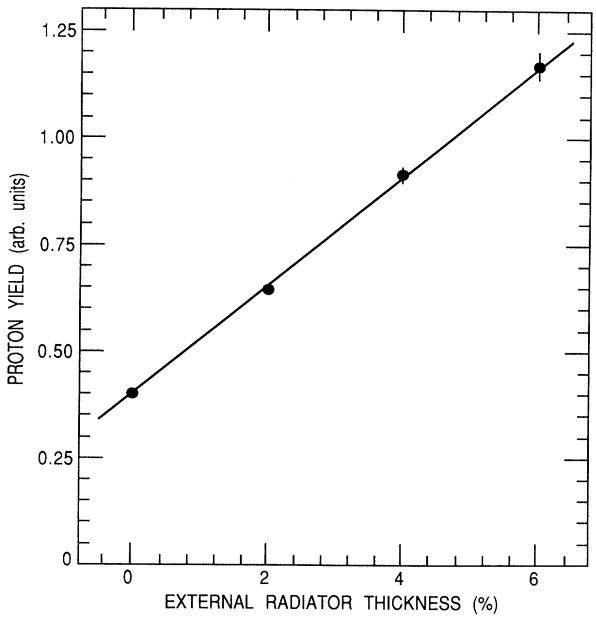

FIG. 5. Proton yield normalized by electron current measured as a function of Cu radiator thickness. The straight line is fit to the data.

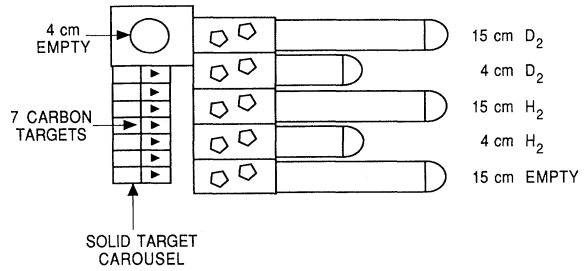

FIG. 6. Side view of the assembly of cryogenic and solid targets used in this experiment. This assembly can be rotated around a vertical axis as well as moved linearly along the vertical direction.

reaction used to make these studies.

The cryogenic targets were designed [21] to handle the high heat load from energy loss of the electron beam in the target. A fan pump generated a high flow rate of the cryogen through a closed circuit including the target cell and a heat exchanger in contact with a reservoir of liquid hydrogen at atmospheric pressure. The cryogen in the circuit was kept at approximately 2 atm pressure to inhibit gas bubble formation in the vicinity of the beam. The pressure and temperature of all cryogenic targets was recorded and used to calculate the density on a run-by-run basis. Typically the density in each target varied by approximately 0.1%. The absolute density was uncertain to about 0.7%, limited by various cryogenic coefficients.

The upstream (downstream) endcaps of the target cells were curved domes of 0.064 mm (0.127 mm) Al. The background proton yield produced from them was a significant fraction of the signal from deuterium for much of the kinematic range. This background was subtracted using the hydrogen-filled cells.

C. Spectrometer

Particles from the target were momentum analyzed and identified using the SLAC 1.6 GeV/c spectrometer instrumented with a new detector package of scintillator hodoscopes in combination with drift chambers plus a threshold Čerenkov detector. The spectrometer has a 90° bend of 254 cm radius in the vertical direction and is weakly focusing. The momentum acceptance is approximately ±5%. The spectrometer is described fully in Ref. [22]. In the present experiment, entrance slits were positioned to limit the solid angle acceptance to approximately 2 msr. An additional set of tungsten slits was used to reduce background from the target endcaps during the measurement of the cross section at 143° center-of-mass angle and 1.6 GeV photon energy, reducing the solid angle acceptance to 1.6 msr.

The magnetic field in the spectrometer is determined by observation of nuclear magnetic resonance, using a remotely controlled probe which could be inserted in the magnet gap to a position approximately at the central ray. The transport matrix for the magnet was taken from earlier calibrations using the floating wire technique [23].

The magnet carriage is attached to a pivot upon which the scattering chamber and targets are mounted, allowing rapid and accurate angle changes. After leaving the target vacuum chamber, scattered particles traverse approximately 1.5 m of air before entering the vacuum chamber of the spectrometer which extends into the shielded detector hut.

D. Detector system

The detector system, shown schematically in Fig. 7, was designed to identify protons and to measure the proton position accurately enough to ensure a momentum resolution of better than 0.5%. The detector system consists of five layers of scintillator hodoscopes, an aerogel Čerenkov counter, and three drift chambers. The performance of this system is discussed in Sec. IV.

1. Scintillator hodoscopes

For momenta greater than around 1 GeV/c, dE/dx alone is not sufficient to separate protons from pions or even positrons. Thus, two techniques were used to ensure that the detected particles were protons: (i) a high-resolution time-of-flight system and (ii) the use of an aerogel threshold Čerenkov counter. The full length of the detector stack was approximately 3 m, and thus, permitted a practical time-of-flight system.

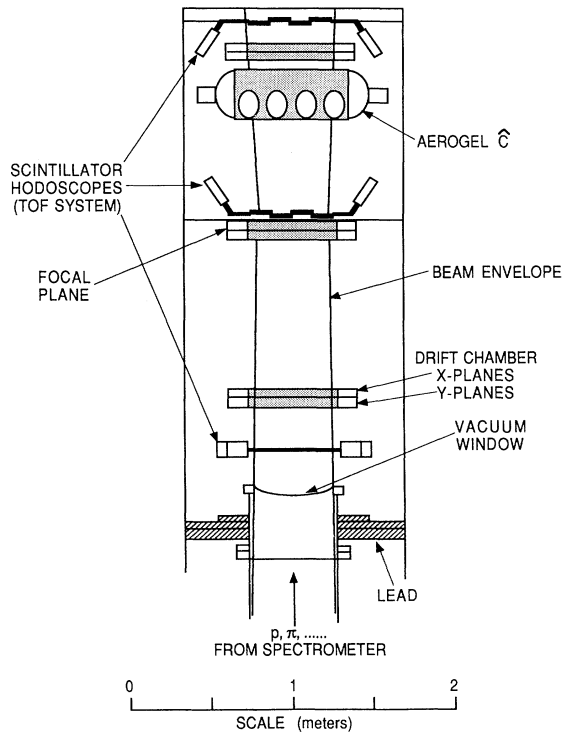

FIG. 7. Instrumentation package of the 1.6 GeV/c spectrometer.

The time-of-flight system made use of the five planes of scintillator hodoscopes as shown in Fig. 7. A plane of eight very thin (1.6 mm thick × 6.0 cm wide × 60 cm long) scintillators was used near the spectrometer vacuum window, the entrance to the detector stack. Fast photomultiplier tubes (Philips XP2230) were fixed directly to each end of each thin scintillator.

Two planes of scintillators (6.4 mm thick × 10.0 cm wide) were located near the focal plane and two planes (6.4 mm thick) were located near the back wall of the shield house. In order to ensure good time-of-flight resolution, a fast photomultiplier tube (RCA 8575) was used on each end of the approximately 60 cm long scintillators. Because of space limitations only one phototube was used for each of the scintillators in the plane nearest the shield-house back wall.

2. Aerogel Čerenkov detector

In addition to the time-of-flight system, an aerogel Čerenkov counter was used to trigger on pions or positrons, having been designed to identify potential π^+ backgrounds in the proton signal. It is made from a simple "diffusion box" design [24], with a 9 cm thick aerogel radiator and viewed by 10 RCA 4522 photomultipliers. The signals from each photomultiplier (PMT) are discriminated and latched, with the discriminator threshold set well below the single photoelectron pulse height. Figure 8 shows the number of photomultipliers that cross threshold with the spectrometer tuned for elastically scattered electrons ($\beta = 1$), and for 520 MeV/c π^+ ($\beta = 0.966$). The inefficiency, i.e., fraction of events with no PMT's over threshold for the electrons is approximately 0.1% which implies roughly seven photoelectrons on average. This is consistent with empirical estimates [24]. The π^+ inefficiency is 13% or around two photoelectrons. This agrees with the quoted index of refraction ($n = 1.05$) and the $\beta = 1$ value obtained from the electrons.

A valid electronics trigger required all four of the thick scintillator planes to fire. The thin scintillator plane and the aerogel counter were not used in the trigger. The aerogel detector confirmed that the π^+ background to $^2\mathrm{H}(\gamma,p)n$ was negligible, and it was not invoked to determine the final yields. However, the detector was used to identify π^+ from the $p(\gamma,\pi^+)n$ reaction. This cross section was compared to previous measurements and served as a check of our procedure.

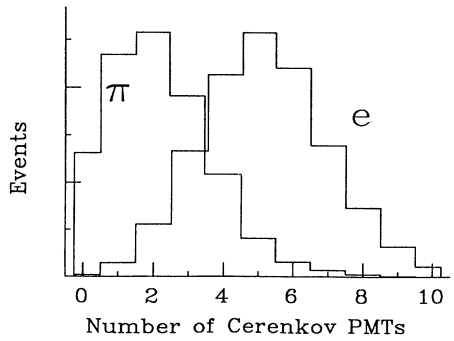

FIG. 8. Response of the aerogel Čerenkov detector to electrons and pions. The horizontal axis is the number of photomultiplier tubes which detected sufficient pulse height to cross threshold.

3. Drift chambers

The three drift chambers were used to determine the trajectories of particles transported through the spectrometer. Each chamber contains two x and two y planes of wires, where the x and y wires are perpendicular to one another. The chambers have an active area of 42 × 62 cm. Wire planes consisted of alternating anode and field wires, with adjacent wires 1 cm apart. Both the anode and field wires consisted of 75-μm diameter gold-plated tungsten wire. A constant flow of 89% Ar, 10% CO_2, and 1% methane was used in the chambers and an average efficiency greater than 98% per plane was achieved for detecting electrons. The two x planes and two y planes were offset from one another by 1 cm in order to eliminate the usual ambiguity of whether the particle passed to the left or right of a given wire.

With an anode wire voltage of typically 1850 V and a field wire voltage of −400 V, the drift times were typically 250 ns/cm. Each anode wire was connected to the "start" of a TDC channel while a valid trigger signal provided a common stop for the time digitizers. The chambers were capable of a spatial resolution of 150 μm, but the actual resolution of the entire spectrometer system was governed by multiple scattering in the vacuum window, first scintillator plane, and the drift chamber materials. Uncorrected for drift time, the chambers yielded a typical spatial resolution of 5 mm, leading to a typical momentum resolution of 0.2%, which was more than adequate for the present experiment.

4. Data acquisition system

Both analog and timing signals were recorded for each phototube on the scintillator hodoscopes and the aerogel counter by using conventional LeCroy 2249A ADC and 2228 TDC CAMAC modules. The trigger provided a common start for the TDC and a gate for the ADC modules. As mentioned above, the trigger provided a common stop for the drift chamber TDC modules.

Between the SLAC electron beam pulses, the CAMAC modules were read out and reset by a dedicated PDP-11 computer. The data were then forwarded to a VAX-780 computer where the data were recorded on tape. To ensure that only one event was processed per beam burst, a 10 μs long veto gate was generated by a trigger to veto possible subsequent triggers. The number of event triggers both with and without the veto were recorded by two scaler channels. The ratio between them was taken as the computer deadtime.

An LSI-11 computer, which communicated with the VAX-780, was used to monitor and control the beam steering, and to read and clear the beam current integrating toroid electronics. The LSI computer returned

cumulative toroid values and beam steering diagnostics at regular intervals to the VAX. Hardware such as the target ladder, spectrometer angle, spectrometer current, and target temperature were monitored and controlled by the VAX through CAMAC interfaces.

E. Method

The cross section at each photon energy and angle was extracted from four separate measurements: (1) Cu radiator and liquid deuterium (LD_2) target in the beam (N_{rd}); (2) Cu radiator and liquid hydrogen (LH_2) target in the beam (N_{rh}); (3) LD_2 target in the beam and no radiator (N_{od}); and (4) LH_2 target in the beam and no radiator (N_{oh}). The yields from each of these experiments were normalized relative to the electron beam current monitors. The yield from photodisintegration of the deuteron was then obtained from the following expression:

$$N_d = (N_{rd} - N_{rh}) - (N_{od} - N_{oh}) \ .$$

The yield measurement with the LH_2 target is a good measure of background, since photoprotons from the $H(\gamma,p)\pi^0$ reaction would be kinematically forbidden at the deuteron end point because of the energy lost to π^0. However, photoprotons were observed from the aluminum target windows. Although the target windows were relatively thin, the yields ranged from 10% of the primary yield at forward angles to 50% of the yield at the largest angles. For the 143° results at 1.6 GeV, a special tungsten mask was added to the spectrometer entry port to preferentially shield the target windows relative to the target. The measurement with the radiator out gives the yield of photoprotons from virtual photons and from bremsstrahlung photons produced in the target. A correction for the distortion of the electron beam passing through the radiator must be taken into account before performing the above subtraction. This is discussed in Ref. [25]. At each electron energy an accompanying measurement of *e-p* elastic scattering was performed, not only as a quick test that all detectors were still working properly, but also as a check of the normalization of the spectrometer solid angle. The *e-p* elastic scattering measurements consisted of both a run in which the electron

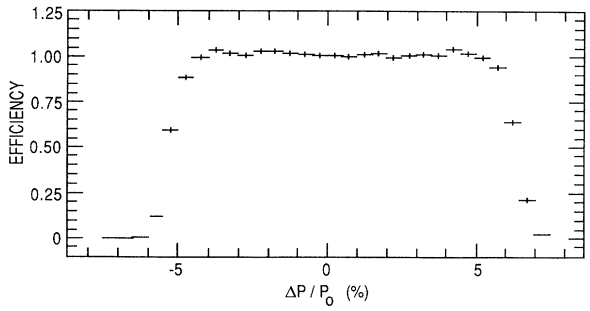

FIG. 9. Momentum acceptance of the spectrometer as a function of $\Delta p/p$ as determined by analysis of quasifree electron scattering from carbon.

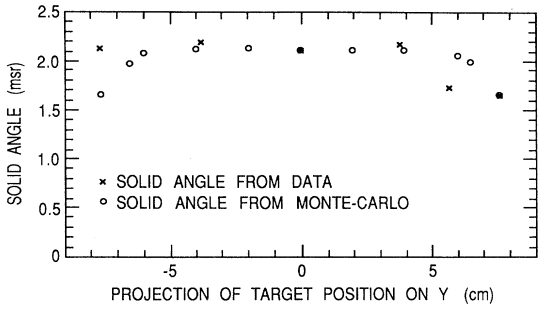

FIG. 10. Solid angle acceptance as a function of target position along the beam direction. The crosses were determined from analysis of quasifree scattering from carbon. The circles are the results of a Monte Carlo simulation.

was detected in the 1.6 GeV spectrometer and a separate run where the scattered proton was detected. This permitted the empirical determination of the proton attenuation in the detector stack as discussed in Sec. IV E.

In addition to the check of the spectrometer solid angle by *e-p* elastic scattering, the momentum acceptance was checked by quasifree electron scattering from carbon. Here, the spectrometer momentum was adjusted to position the quasifree peak for $^{12}C(e,e')$ at six points along the focal plane of the spectrometer. By knowing the approximate shape of the quasifree peak, the momentum acceptance of the spectrometer could be deduced. The result of this procedure is shown in Fig. 9. As expected, the momentum acceptance of the spectrometer is nearly momentum independent from -4% to $+5\%$. This result is in excellent agreement with the Monte Carlo model for the spectrometer. Although the 1.6 GeV spectrometer was designed for use with extended targets, the effect of target length on the spectrometer acceptance was measured, using the carbon targets described in Sec. III B. The full extent of the LD_2 and LH_2 targets was ± 7.5 cm. A sequential set of runs for quasifree scattering from the series of carbon targets was used to determine the target length acceptance of the spectrometer. The results of this test are presented in Fig. 10, and show that the acceptance of the spectrometer is unchanged from -7.5 to $+4.0$ cm with a dropoff in solid angle of approximately 20% for $+7.5$ cm. This amounts to an overall correction to the solid angle of $< 3\%$ as discussed in Sec. IV E.

IV. REDUCTION AND ANALYSIS OF DATA

The primary data reduction and analysis were performed off line. The goal was to determine yields as a function of proton momentum and scattering angle, binned over the spectrometer acceptance. Individual rays must first be tracked through the drift chambers so that we can calibrate and invoke the particle identification system, and subsequently determine the proton's momentum and scattering angle. In the following subsections we describe how these tasks were accomplished, followed by a discussion of the various corrections we need to apply and the ensuing systematic uncertainties implied for the yields. More details are available [25].

A. Tracking

The particle tracking begins with pattern recognition based on the hodoscope counters and drift chambers. For the top and middle drift chambers (see Fig. 7) we only considered wires that were overlapped by corresponding scintillators in the adjacent hodoscope plane. The bottom drift chamber was located too far from the bottom hodoscope to allow this masking to be imposed.

Drift chamber data were preferentially used if they corresponded to two adjacent wires whose combined drift time was consistent with a single particle traversing the drift chamber. In this case, the position was obtained from a linear extrapolation between the two wires based on the drift times. If no wire pair was identified within the hodoscope mask, we considered single wires within the mask. In cases where there was more than one candidate drift chamber coordinate in any plane, we decided among the various combinations by taking the one which resulted in a minimum χ^2 for a straight line fit. A very loose χ^2 cut, roughly 18 for 7 degrees of freedom based on a common position uncertainty of ± 0.5 cm, was imposed.

B. Particle identification

We identified protons primarily using time of flight (TOF). The scintillator hodoscopes were calibrated for TOF measurements using $\beta = 1$ electrons obtained during dedicated electron scattering runs with LH_2 or ^{12}C targets. An iterative procedure was used to determine the collective timing offsets for each channel due to differences in cable lengths and photomultiplier transit times. An empirical pulse height correction was applied based on the measured time deviations as a function of the pulse height digitized by the corresponding ADC. Time resolution on the order of ± 200 ps (rms) was obtained for the 6.4 mm thick scintillators, and around ± 350 ps for the 1.6 mm thick layer.

Particle velocity was determined by using the time from each intercepted scintillator along the track. The fitted slope, including the track inclination angle, was converted to velocity. A maximum of 8 time measurements was possible (the uppermost hodoscope layer was excluded since it determines the trigger time), but we allowed as few as four valid time signals. A very loose χ^2 cut was imposed. The velocity could be determined for more than 99% of the tracked events.

The spread in proton velocities due to the momentum acceptance of the spectrometer is significant and contributes to the velocity resolution, especially for the lower momenta. Therefore, we determine the apparent particle mass on an event-by-event basis using the reconstructed momentum in the spectrometer (see Sec. IV C). The resulting mass spectrum is shown in Fig. 11 for a nominal central momentum of 1.45 GeV/c which is the most difficult case from the point of view of particle identification. The separation from deuteron and triton background (from the aluminium target windows) is sufficient.

There is evidently no significant π^+ contamination to the data as seen in Fig. 11 and the separation between protons, deuterons, and tritons is already quite good. Therefore, scintillator dE/dx and the aerogel Čerenkov detector were not used in the final analysis.

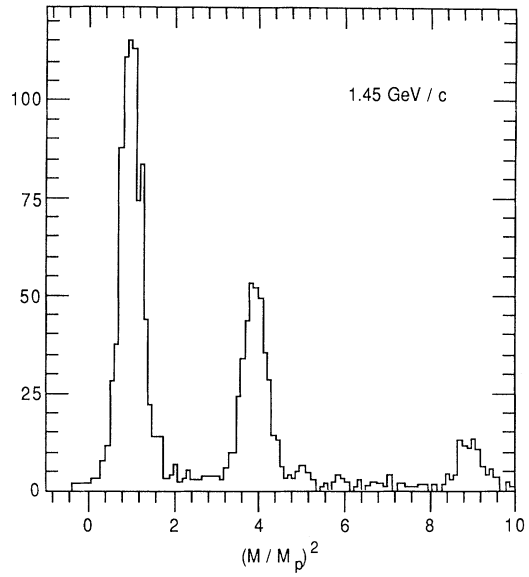

FIG. 11. Particle mass squared, as determined from spectrometer momentum and time of flight within the detector stack, for the maximum momentum of the spectrometer.

C. Momentum and scattering angle reconstruction

The 1.6 GeV/c spectrometer focuses momentum in the bend plane and scattering angle (the proton angle with respect to the incident photon direction) in the transverse plane. The focal plane is nearly normal to the central ray and lies very close to the middle drift chamber in Fig. 7. Therefore a reasonable first approximation to the momentum and scattering angle (relative to the central values) is given by the x and y positions in that drift chamber. However, we can correct for the various aberrations using the actual particle trajectories as determined by tracking. This improves the resolutions so that they are limited by the beam energy spread and multiple scattering. We used a "reverse transformation" matrix determined using a wire float technique [23] to correct the abberations using the track parameters.

D. Normalization and determination of differential cross section

Having determined the number of protons with particular momentum and scattering angle, we extract the net yield for protons photoproduced in deuterium using the subtraction method described in Sec. III E. We now must extract the yield for the $^2H(\gamma,p)n$ reaction and normalize it to determine the differential cross section.

The proton momentum and scattering angle are correlated by kinematics, and we use this to identify protons from $^2H(\gamma,p)n$. Assuming the reaction is $^2H(\gamma,p)n$, we can reconstruct the photon energy E_γ from the proton

momentum and angle. In the absence of yield from any other processes, the yield as a function of E_γ will be the cross section times the bremsstrahlung spectrum for $E_\gamma \leq E_0$, the beam energy. The net yield should subtract to zero for $E_\gamma \geq E_0$.

Figure 12 shows the yields versus $E_\gamma - E_0$ for three of our kinematic settings, namely, $\theta_{\text{c.m.}} = 90°$ with (a) $E_0 = 0.8$ GeV, (b) $E_0 = 1.6$ GeV, and (c) $\theta_{\text{c.m.}} = 143°$ with $E_0 = 1.6$ GeV. The bremsstrahlung end-point shape is clearly evident in each case. The fits use a standard bremsstrahlung shape and a nominal energy dependence for the cross section, folded with the experimental resolution. They demonstrate consistency in the analysis, but are not used to derive the cross section. For the forward angle measurements, i.e., $\theta_{\text{c.m.}} = 90°$ where the proton laboratory momentum is relatively high, the yield past the end point nearly subtracts to zero. This is not the case, however, for the backward angle measurements. This additional yield is primarily from the two-step reaction $^2\text{H}(\gamma,\pi^\pm)X$ followed by $^2\text{H}(\pi^\pm,p)X$ and tends to populate the data sets at backward angles where the photoproton momentum is relatively low [Fig. 12(c)]. This background is calculated [25] by folding a bremsstrahlung photon energy distribution with the measured pion photoproduction, scattering, and absorption cross sections, integrating over all intermediate angles and energies which could result in a proton in the acceptance of the spectrometer. The result, normalized to the yield above the photodisintegration end point, is shown in Fig. 12(c). The model agrees well with the energy dependence of the yield past the kinematic end point for $^2\text{H}(\gamma,p)n$. It also indicates a nearly energy-independent contribution to the total yield below the end point, thus one can reliably extract the yield for $^2\text{H}(\gamma,p)n$.

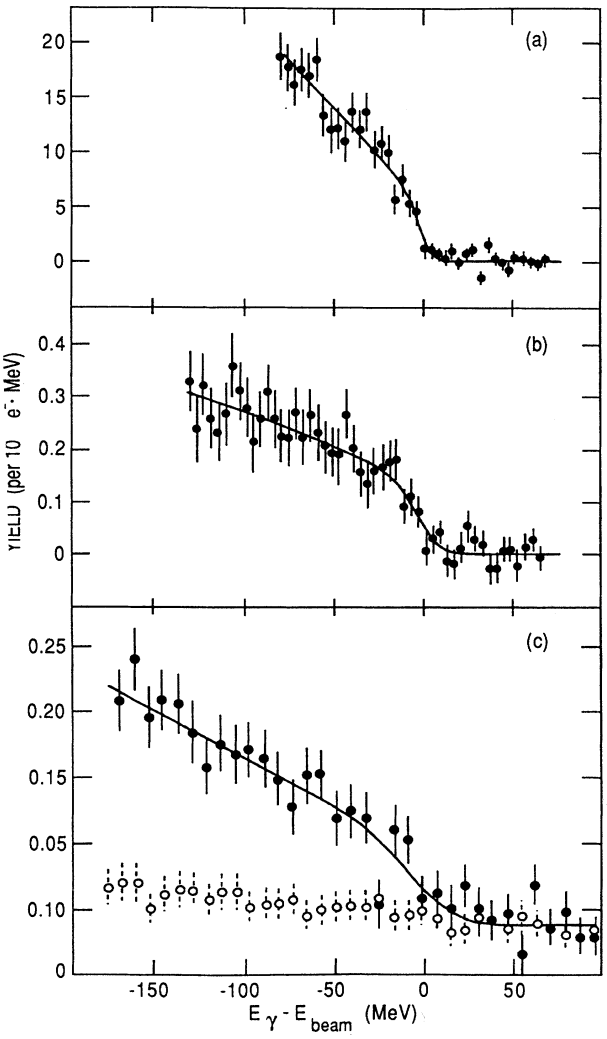

FIG. 12. Subtracted proton yields as a function of E_γ for the reaction $^2\text{H}(\gamma,p)n$ for (a) $E_\gamma \approx 0.8$ GeV and $\theta_{\text{c.m.}} = 90°$, (b) $E_\gamma \approx 1.6$ GeV and $\theta_{\text{c.m.}} = 90°$, and (c) $E_\gamma \approx 1.6$ GeV and $\theta_{\text{c.m.}} = 143°$. The solid lines are fits using a thick target bremsstrahlung calculation, folded with the experimental resolution, along with a nominal energy dependence of the cross section.

Each of the many E_γ spectra, of the type shown in Fig. 12, is used to determine the differential cross section $d\sigma/d\Omega$ at two photon energies. The energy region between the π^0 production threshold and 25 MeV below the end point is divided into two approximately equal bins. We then determine the laboratory cross section using

$$\left(\frac{d\sigma}{d\Omega}\right)_{\text{lab}} = \frac{Y}{N_{\text{tgt}} N_\gamma \Omega_{\text{eff}}}$$

where Y is the proton yield in one of the two bins, N_{tgt} is the number of target deuterons, and Ω_{eff} is the effective solid angle (see Sec. III C), and N_γ is the number of incident photons integrated over this energy bin. The laboratory cross section is converted to the c.m. system using the calculated Jacobian and the central angles and momenta of the spectrometer. The calculation of the photon flux is described in Sec. III A.

E. Corrections

A number of corrections to the final yield were necessary to obtain the final cross sections. These corrections included tracking efficiency of the drift chambers, proton attenuation in the detector stack, extended target length corrections to the spectrometer solid angle, computer deadtime, and target purity. These corrections are discussed briefly below.

Since the tracking algorithm is not 100% efficient, it was necessary to measure the efficiency and make a correction to the yield. The efficiency was determined by using only real proton events, i.e., those events which pass the mass and dE/dx cuts. Then, fiducial cuts on the active volume were used to further define the useful detector volume. It was estimated that approximately 5% of the true events were lost when a cut in χ^2 on the track fitting was introduced. Although the relative loss was remarkably constant from run to run, the correction was determined for each run. This correction is independent of proton attenuation in the detector stack, since only protons which triggered the final scintillator in the

detector stack were used in the efficiency determination. We applied a small correction for proton loss due to interactions in the detector stack.

The target length used in the present experiment was 15 cm. Two methods were used to determine the effective solid angle for an extended target: (1) yields from a series of carbon targets were measured for a number of locations along the beam axis and (2) a Monte Carlo model of the spectrometer was used to calculate the solid angle for a point target at points along the extended target length. The Monte Carlo model indicated that no correction was needed when the effective target length was less than ± 6.1 cm from the target center (see Fig. 10). The correction to the solid angle for a 15 cm target and the spectrometer set at 90° was 2.7% from the $^{12}C(e,e')$ data and 2.3% from the Monte Carlo analysis. Given this small effect and the small discrepancy between the two methods, the Monte Carlo model was used to correct the solid angle as a function of the spectrometer angle.

Both computer and electronics deadtime were considered in the analysis. The data acquisition system was limited to one trigger per beam pulse by disabling the computer interrupt for approximately 10 μs while an event was being processed. The discrepancy between the number of triggers and the number of events on tape was caused by computer deadtime. The extracted yields were then scaled by the correction factor obtained from the ratio between the event scaler and the trigger scaler. This correction was typically a few percent and was only 10% in the worst case. The electronics deadtime was estimated from the gate widths of the electronics, typically 40 ns, and the actual counting rates. The electronic deadtime was found to range between only 0.1 and 0.3%, and thus was only included as a possible systematic error rather than a correction.

The purity of atomic deuterium in the target was analyzed and found to be 98.3% deuterium, the main contaminant being hydrogen. The cross sections for the $^2H(\gamma,p)n$ reaction were corrected accordingly. Previous experience with the LD_2 and LH_2 targets at SLAC indicated that the beam currents used during this experiment gave a negligible target density decrease due to beam heating. The average beam current was typically not more than 5 μA.

F. Systematic uncertainties

The largest systematic errors arise from the determination of spectrometer solid angle, acceptance function, and the photon flux. These errors were estimated to be $\leq$ 4.6%, 2%, and 3%, respectively, and are shown along with other systematic errors in Table I. For measurements of the $^2H(\gamma,p)n$ reaction at $\theta_{c.m.} = 143°$ and $E_e = 1.6$ GeV, the systematic uncertainty in the background subtraction was approximately 3%. Other notable sources of systematic error were introduced by the radiator in-and-out subtraction technique, target length acceptance, particle identification, and other software cuts. Each of these errors was estimated to be about 1%. Much smaller contributions to the systematic error are also listed in Table I and arose from uncertainties in the electron beam energy, the charge integration technique, measurements of radiator and target thickness, target density and impurity corrections, electronics deadtime, and tracking efficiency.

TABLE I. Summary of systematic uncertainties in $d\sigma/d\Omega$.

Solid angle determination (systematic)	$\leq$4.6%
Solid angle determination (statistical)	1%
Bremsstrahlung calculation	3%
Acceptance function	2%
Software cuts	$\leq$2%
Target length	1%
Radiator-out subtraction	1%
Particle identification	$\leq$1%
Beam current integration	$\leq$0.6%
Radiator thickness	0.5%
Tracking efficiency	$\leq$0.5%
Electron beam energy	0.3%
Momentum calibration	0.3%
Electronic deadtime	$\leq$0.3%
Target density	0.7%
Target impurity	0.1%
Two-step background subtraction $\theta_{c.m.} = 143°$	3%
Total	$\leq$6.6%
Total for $\theta_{c.m.} = 143°$	$\leq$7.2%

Only the estimates of the largest sources of systematic error will be discussed here; further details are available [25]. The effective spectrometer solid angle was measured by performing e-p elastic scattering measurements and comparing these results to the well-known cross sections. As already discussed, the effective solid angle also includes the detector efficiency for protons. Thus, the systematic uncertainty in the effective solid angle includes the systematic error in the e-p scattering measurement, the possible error in the known e-p cross section with radiative corrections, the uncertainty in the proton detection efficiency estimate, and the systematic error in the target length corrections.

The overall systematic uncertainty for the e-p elastic scattering measurement was estimated to be approximately 3.5%. The largest contribution, 2%, arises from software cuts. This uncertainty was estimated by varying the software cuts over acceptable ranges and determining the change in the yield of detected electrons in the spectrum.

Uncertainties in the radiative corrections were estimated [25] to be 2%, and so the uncertainties in the known e-p scattering cross sections were taken to be 2%. The uncertainties in the beam energy (0.1%) and scattering angle (0.05°) contributed up to 0.5% and 0.9%, respectively, to the known cross section.

The correction for proton attenuation in the detector stack was estimated by consideration of measured proton reaction cross sections and the composition and thickness of each detector stack element. Since these corrections were less than 6%, a conservative estimate of the systematic uncertainty of 2% was made for the efficiency of the proton detector. This effect was also checked experimentally by performing e-p elastic scattering measurements in which the proton rather than the electron was de-

tected. At all electron energy settings below 1.6 GeV, the effective solid angle from measurements of the H(e,e')H reaction with the proton efficiency correction was within 3% of measurements of the solid angle with the H(e,p)e reaction. This additional check gives confidence in the determination of the effective solid angle and its uncertainty. This comparison could not be performed with sufficient accuracy above 1.6 GeV because of the large background of photoprotons from the $H(\gamma,p)\pi^0$ reaction near the e-p elastic peak.

The net systematic uncertainty for the $^2H(\gamma,p)n$ cross section as summarized in Table I is less than 6.6%, or less than 7.2% for $\theta_{\rm c.m.} = 143°$. The overall uncertainty in the yield depended on errors in charge integration, target length, impurity and density, electronics deadtime, tracking efficiency, particle identification cuts, analysis errors, and background subtraction. This systematic error in yield amounted to approximately 2.8%. The error in photon flux included not only the error in calculating the bremsstrahlung yield, but also the errors in the radiator thickness measurements. At 143° there was an additional error of 3% owing to the uncertainty in the estimates of subtracting a calculated shape for the two-step background which was discussed in Sec. IV D. The net uncertainty is comparable to the statistical errors in the cross section measurement.

V. PRESENTATION AND DISCUSSION OF RESULTS

Our final measured differential cross sections, $d\sigma/d\Omega_{\rm c.m.}$, are tabulated in Table II. Here $\theta_{\rm c.m.}$ refers to the proton angle with respect to the incoming photon, and the quoted errors are statistical only. The energy dependences of the photodisintegration differential cross section at three different c.m. angles, 90°, 114°, and 143° are displayed in Fig. 13. Previous measurements [26–28] at lower photon energies are also displayed. The results of the present experiment appear to be in agreement with those of Ching and Schaerf [28] at common photon energies (note only statistical uncertainties are indicated). As mentioned earlier, it was possible to subdivide the momentum acceptance of the spectrometer resulting in cross sections at separate photon energies. While independent statistically, these pairs of measurements have some closely correlated systematic uncertainties.

The primary characteristic of the data is the rapid monotonic decrease with increasing photon energy. As a means to examine this more closely, and in light of the predictions of constituent counting rules, the invariant cross section $d\sigma/dt$ has been calculated, where

$$\frac{d\sigma}{dt} = \frac{2\pi s}{E_\gamma M_d [s(s-M_d^2)]^{1/2}} \frac{d\sigma}{d\Omega_{\rm c.m.}}$$

and s and t are the usual Mandelstam variables. The invariant cross section is then multiplied by the factor of s^{11} predicted by the counting rules, and plotted as a function of photon energies for the three different c.m. angles shown in Fig. 14. The scaling of the cross sections is indicated by their approach to a constant, loosely illustrated by the arbitrarily normalized dashed line in each figure. The energy dependence at 90° and 114° does indeed suggest that the power of the s dependence is 11, however the 143° data do not fall as fast or suggest any approach to such a dependence. A fit of the form $d\sigma/dt = A/s^n$ for photon energies above ≈ 1 GeV yields $n = 11.6 \pm 0.3$ at $\theta_{\rm c.m.} = 90°$ (six points), $n = 12.1 \pm 0.2$ at $\theta_{\rm c.m.} = 114°$ (eight points), and $n = 9.4 \pm 1.0$ at $\theta_{\rm c.m.} = 143°$ (four points). The counting rule arguments assume that one has entered an energy region where mass scales of the components are not important, and the s^{-11} dependence should be true at all angles. Thus the disagreement at 143° suggests the scaling regime has not been reached

TABLE II. Measured cross sections (nb/sr) for $^2H(\gamma,p)n$.

Beam energy	Low photon energy bin			High photon energy bin		
E_0 (GeV)	E_γ (MeV)	$\theta_{\rm c.m.}$ (deg)	$d\sigma/d\Omega_{\rm c.m.}$	E_γ (MeV)	$\theta_{\rm c.m.}$ (deg)	$d\sigma/d\Omega_{\rm c.m.}$
0.808	744	52.4	194±15	768	52.7	173±14
	740	77.6	198±9	766	78.0	162±8
	739	89.0	227±9	767	89.5	178±8
	728	112.4	193±10	762	113.0	144±8
	724	125.8	168±10	761	126.4	117±8
	713	142.1	143±9	757	142.6	99±8
1.007	927	65.5	55.4±3.1	960	65.9	45.0±3.1
	926	77.6	59.4±3.0	960	78.0	44.0±2.6
	924	89.0	58.0±2.9	962	89.5	58.2±2.5
	915	112.4	56.0±3.3	957	113.0	46.7±2.9
	920	125.0	50.4±2.9	960	126.4	41.7±2.7
	913	142.3	46.4±3.9	957	142.7	41.6±3.6
1.200	1111	65.4	24.0±1.4	1150	65.8	20.0±1.1
	1109	88.9	22.6±0.7	1151	89.4	17.6±0.6
	1109	112.5	21.5±0.7	1151	113.0	17.7±0.6
	1107	142.3	22.4±1.3	1148	142.7	20.1±1.3
1.402	1298	89.0	9.1±0.5	1343	89.5	6.7±0.4
	1310	112.6	6.9±0.4	1350	113.1	6.4±0.4
	1309	142.4	12.0±0.8	1351	142.7	10.6±0.8
1.603	1507	88.9	4.0±0.2	1553	89.4	3.7±0.2
	1505	112.6	3.6±0.2	1549	113.1	2.7±0.1
	1512	142.5	6.5±0.6	1551	142.8	5.5±0.6
1.793	1695	112.6	1.9±0.1	1738	113.0	1.6±0.1

at these photon energies. We point out, however, that the fitted values of n depend rather strongly on which data points are included. For example, if we only fit the *six* highest energy points at $\theta_{\text{c.m.}} = 114°$, we obtain $n = 10.5 \pm 0.4$.

The reduced nuclear amplitudes model of Brodsky and Hiller [7] predicts that one can find a measure of the cross section, $f^2(\theta_{\text{c.m.}})$, which will scale assuming "constituent" nucleons, if one removes the form factors of the nucleons themselves. Figure 15 displays this function for three angles. As in the previous figure, the predicted scaling behavior is indicated schematically by the dashed line. None of the angles exhibits the scaling of the reduced amplitude, which has been successful in describing elastic electron scattering at large momentum transfer. While one can argue that the momentum transfer to one of the nucleons becomes too small at angles far from 90° and one should not expect scaling in this model, still the 90° energy dependence does not convincingly suggest scaling of the kind described in Ref. [7].

Lee's calculations [13] of the differential cross section are also compared with the data in Figs. 13, 14, and 15. At lower photon energies, they appear to fall systematically below the observed cross sections, the most severe disagreement being at $\theta_{\text{c.m.}} = 90°$ near $E_\gamma = 650$ MeV. The magnitude of the data is better described around 800 MeV, but above 1 GeV the calculation is clearly in disagreement with the cross sections in both magnitude and dependence on photon energy. Interestingly, at 90° and 114° Lee's results fall less slowly than the data, while at the furthest backward angle, the theoretical cross sections fall more rapidly. Lee [29] attributes the high photon energy dependence to final state interactions (FSI) among the outgoing hadrons, which in combination with the comparison to data suggests the calculated FSI are too strong. However, other effects such as higher mass baryon resonances and heavy-meson exchange have not been included and these are speculated to be the cause of the observed discrepancy.

Continuing the focus on calculations based on the meson-baryon picture, Fig. 16 compares the available theoretical results from several other groups to the energy dependence at 90°. The solid curve indicates the predictions of Kang *et al.* [15] and can be seen to provide much

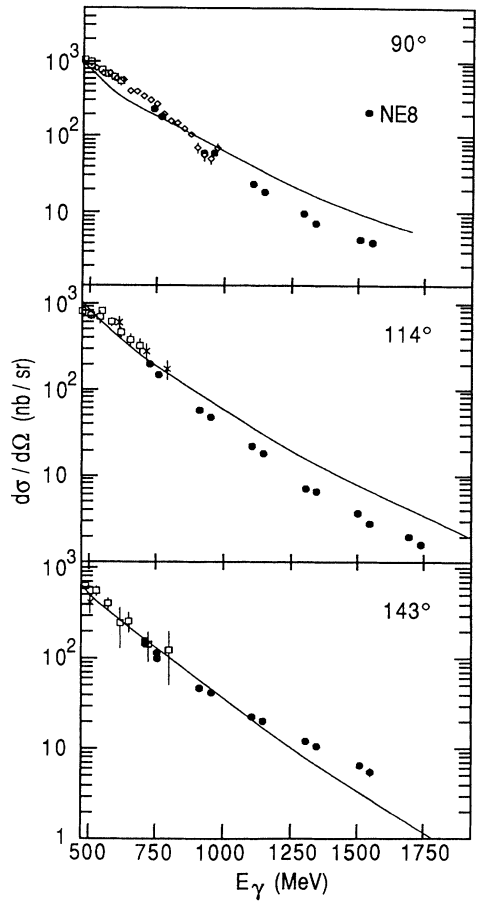

FIG. 13. Photon energy dependence of the disintegration cross section $d\sigma/d\Omega_{\text{c.m.}}$ for center-of-mass (c.m.) angles 90°, 114°, and 143°. Squares are data from Ref. [26], crosses from Ref. [27], diamonds from Ref. [28], and circles from the present experiment. The solid curves are theoretical predictions from Ref. [13]. Only statistical errors are included.

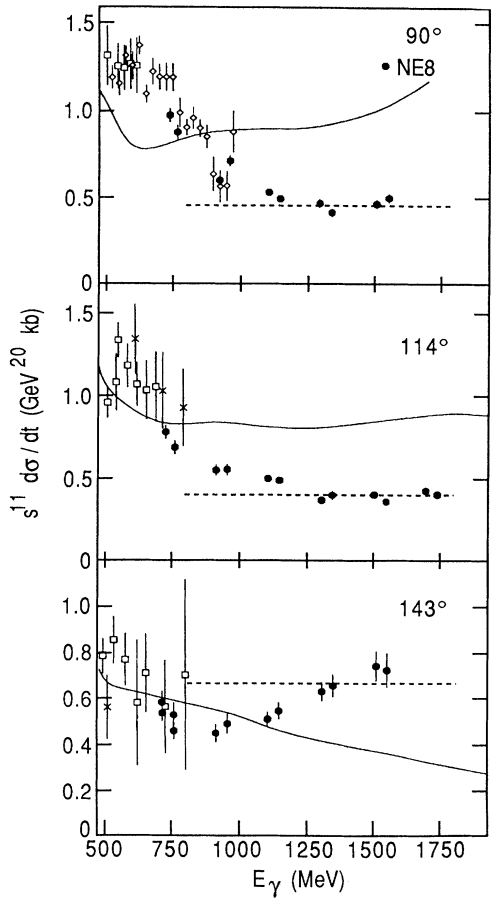

FIG. 14. Photon energy dependence of the disintegration cross section $d\sigma/dt$ scaled by the expected s^{11} dependence. (See text for discussion.) The data and solid curve are as in Fig. 13. The dashed line is arbitrarily normalized.

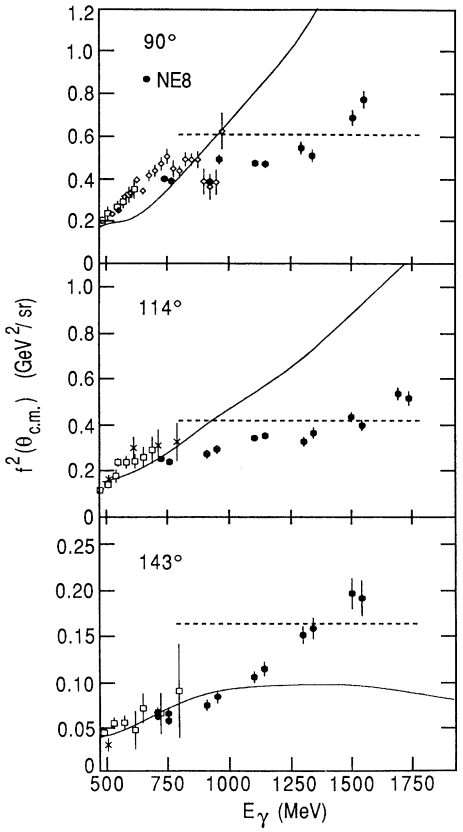

FIG. 15. Photon energy dependence of the reduced nuclear amplitude squared for the photodisintegration reaction. The data and solid curve are as in Fig. 13. The dashed line is arbitrarily normalized.

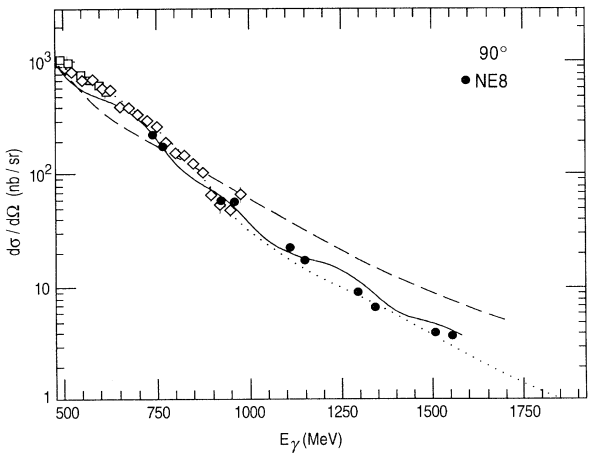

FIG. 16. Energy dependence of the differential cross section $d\sigma/d\Omega_{c.m.}$ at center-of-mass angle 90°. The solid curve is the prediction of Ref. [15], the dashed curve is the prediction of Ref. [13], and the dotted curve is the prediction of Ref. [16]. The data are as in Fig. 13. Reference [16] is normalized to the data at 1 GeV.

better agreement than the results of Lee (dashed curve). The dotted curve represents the results of Nagornyĭ *et al.* [16] which are perhaps slightly better in agreement with the data than those of Kang *et al.*. However, the Nagornyĭ *et al.* calculation has been normalized to the cross section at 1 GeV and is therefore essentially a prediction of the energy dependence alone. The success of these two different calculations is somewhat surprising given their very different dynamical content. The model of Kang *et al.* includes many baryon resonances, exchange of three different mass mesons with accompanying form factors at the meson-baryon vertices and FSI. In contrast, Nagornyĭ *et al.* contains no explicit meson terms, no FSI, and an amplitude derived from the relativistic structure of the interaction of the photon with nucleons without excitation to other baryon states. (Reference [16] contains other results allowing excitation of the Roper(1440) resonance, which are not shown here.) Mesons enter only through the form factors at the nucleon-photon vertices. Given these differences, the agreement with the steep energy dependence of the cross section supports the authors' claims that models based on a meson-baryon picture are able to provide the required fall with s, although perhaps not predict it. It should also be mentioned here that an additional model [30], based on Regge phenomenology, has also been able to describe the magnitude and perhaps the observed s dependence of the 90° cross sections at the very highest energies at which they were measured. Low photon energy data were used to fix parameters in the model, but further measurements are required to test it. While the authors' note that the Regge picture includes processes and deuteron structures not contained in the meson-baryon models, the apparently small relative values of these quark-gluon effects does not provide much hope for their elucidation at these energies.

Nagornyĭ *et al.* also suggest that the angles near 90° are especially given to this scaling behavior because of the cancellation of interference terms between the electric and magnetic parts of the photon-deuteron interaction. They further predict that at forward and backward angles, the cross section will not fall as rapidly as s^{11} for any accessible value of s. This is indeed born out by the 143° energy dependence. Whether their predictions can survive in a model required to predict the magnitude of the cross section is unknown. Possibly this is in part the reason that Kang *et al.* are required to include more physical processes in order to describe the 90° cross section. Unfortunately, the monopole form factors used for computational reasons in the latter calculation make it difficult to judge the predictive power of the model, and therefore theoretical results at additional proton angles and incident photon energies would be very useful.

Because of the upper limit on the momentum in the 1.6 GeV/c spectrometer, complete measurements of the angular distributions of the differential cross section up to high photon energies were not performed. Nonetheless, those cross sections measured are presented as a function of c.m. angle in Fig. 17. Little structure is seen at the lowest energies, though one sees that the new data are in agreement with earlier measurements. The most

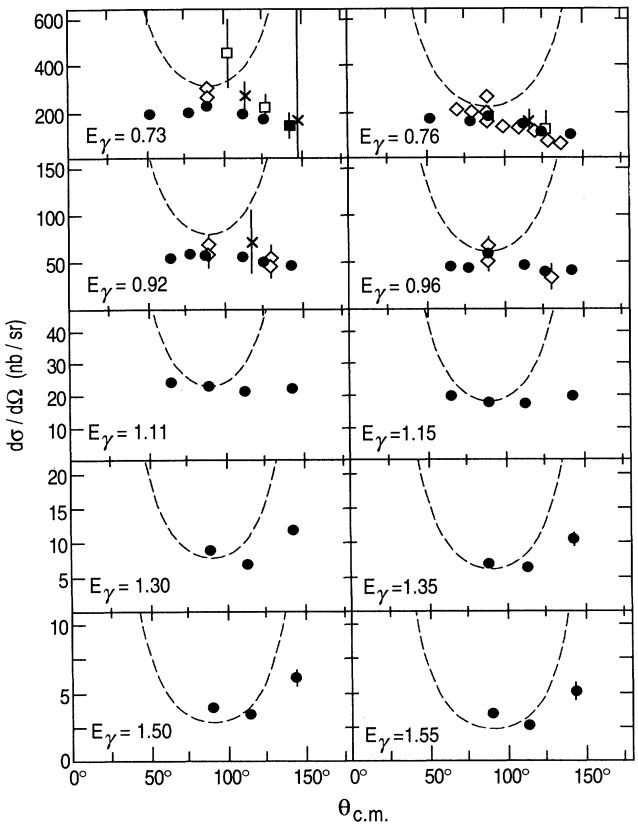

FIG. 17. Angular distribution of the differential cross section $d\sigma/d\Omega_{\text{c.m.}}$. The data are as in Fig. 13. The dashed curve is the prediction based on the model of Brodsky and Hiller [7], and we assume the unknown function $f^2(\theta_{\text{c.m.}})$ is an arbitrary constant.

striking feature is the rise of the backward cross section as photon energy increases, or in another sense, its less rapid fall with increasing energy. As mentioned above, this behavior has been predicted by Nagornyĭ *et al.* [16]. If one assumes a constant value of the reduced nuclear amplitude $f^2(\theta_{\text{c.m.}})$ described by Brodsky and Hiller [7], one can then use the form factors to find the angular distribution (in Fig. 17 a value of unity has been assumed). A strong forward or backward peaking of the cross section results. As mentioned above, this is the effect of the momentum transfer being soft to either the proton or the neutron at forward or backward angles, respectively, leading to larger cross sections as a result of the evaluation of the nucleon form factors at the lower momentum transfer.

VI. SUMMARY

An experimental investigation of the two-body disintegration of the deuteron has been extended to 1.8 GeV in photon energy, almost doubling the energy range of the existing measurements. The energy dependence of the cross section at $\theta_{\text{c.m.}} = 90°$ suggests that scaling predicted by constituent quark-counting rules may have begun, but at least one calculation based on a meson-baryon reaction model is also able to describe the energy dependence as well as the magnitude of the cross section. The energy dependence of the reaction at 143° does not exhibit the predicted scaling, suggesting that this energy regime has not yet been reached. The reduced nuclear amplitude model of Brodsky and Hiller which attempts to move scaling down to lower energies does not appear to describe well the energy dependence of the data, although there is some degree of agreement with the angular dependence.

The theoretical understanding of the reaction is still unclear, since two very different meson-baryon models are able to describe the energy dependence. More data over a broader range of angle and incident energy are necessary to truly constrain and test the models. Recently, some further measurements have been performed at SLAC (experiment NE17) which extend to over 4 GeV in photon energy and also determine the energy dependence at a forward angle ($\theta_{\text{c.m.}} = 37°$). In the near future, a more systematic exploration, approved at CEBAF, should provide a much better testing ground for the theoretical calculations.

ACKNOWLEDGMENTS

We gratefully acknowledge the help of the SLAC staff as well as R. Arnold and Z. Szalata. Discussions with T.-S. H. Lee have been particularly useful. This research was supported in part by the U.S. Department of Energy, Nuclear Physics Division, under Contract Nos. W-31-109-ENG-38, DE-A505-76-ERO-4043, DE-AC02-76-ERO-3069, and DE-FG03-88-ERO-4039, and by the National Science Foundation under Grant Nos. PHY85-05682, PHY86-08247-01, and PHY87-15050.

[1] J. Napolitano *et al.*, Phys. Rev. Lett. **61**, 2530 (1988).
[2] R. G. Arnold *et al.*, Phys. Rev. Lett. **57**, 174 (1986).
[3] R. L. Anderson *et. al.*, Phys. Rev. D **14**, 679 (1976).
[4] V. A. Matveev, R. M. Muradyan, and A. N. Tavkhelidze, Lett. Nuovo Cimento **7**, 719 (1973).
[5] S. Brodsky and G. Farrar, Phys. Rev. Lett. **31**, 1153 (1973).
[6] R. J. Holt, Phys. Rev. C **41**, 2400 (1990).
[7] S. J. Brodsky and J. R. Hiller, Phys. Rev. C **28**, 475 (1983).
[8] S. J. Brodsky and B. T. Chertok, Phys. Rev. D **14**, 3003 (1976).
[9] N. Isgur and C. H. Llewellyn-Smith, Nucl. Phys. **B117**, 526 (1989).
[10] R. B. Wiringa, R. A. Smith, and T. L. Ainsworth, Phys. Rev. C **29**, 1207 (1984); R. Machleidt, K. Holinde, and Ch. Elster, Phys. Rep. **149**, 1 (1987); M. Lacombe *et. al.*, Phys. Rev. C **21**, 861 (1980); M. M. Nagels, T. A. Rijken, and J. J. DeSwart, Phys. Rev. D **17**, 768 (1978).
[11] H. Arenhovel and M. Sanzone, *Few Body Systems* (Springer-Verlag, Berlin, 1991), Suppl. 3.
[12] J. M. Laget, Nucl. Phys. **A312**, 265 (1978).

[13] T.-S. H. Lee, Argonne National Laboratory Report PHY-5253-TH-88, 1988; T.-S. H. Lee, *Proceedings of the International Conference on Medium and High Energy Nuclear Physics*, Taipai, Taiwan, 1988 (World Scientific, Singapore, 1988), p. 563.
[14] T.-S. H. Lee, Phys. Rev. C **29**, 195 (1984).
[15] Y. Kang, P. Erbs, W. Pfeil, and H. Rollnik, *Abstracts of the Particle and Nuclear Intersections Conference*, (MIT, Cambridge, MA, 1990); W. Pfeil (private communication).
[16] S. I. Nagornyĭ, Yu. A. Kasatkin, and I. K. Kirichenko, Yad Fiz. **55**, 345 (1992) [Sov. J. Nucl. Phys. **55**, 189 (1992)].
[17] F. Gross and B. D. Keister, Phys. Rev. C **28**, 823 (1983).
[18] NPAS Users Guide, Report No. SLAC-REP-269, 1984 (unpublished), p. 14.
[19] J. L. Matthews and R. O. Owens, Nucl. Instrum. Methods **111**, 157 (1973).
[20] J. L. Matthews, D. J. S. Findlay, and R. O. Owens, Nucl. Instrum. Methods **180**, 573 (1981).
[21] John W. Mark, in *Advances in Cryogenic Engineering*, edited by R. W. Fast (Plenum Press, New York, 1983), Vol. 29, p. 1033.
[22] R. Anderson, D. Gustavson, R. Prepost, and D. Ritson, Nucl. Instrum. Methods **66**, 328 (1968).
[23] W. B. Atwood, SLAC Report No. SLAC-REP-185, 1975 (unpublished).
[24] P. Carlson, Nucl. Instrum. Methods A **248**, 110 (1986).
[25] T.-Y. Tung, Ph.D. thesis, Northwestern University, 1992 (unpublished).
[26] P. Dougan *et. al.*, Z. Phys. A **276**, 55 (1976).
[27] H. Myers, R. Gomez, D. Guinier, and A. V. Tollestrup, Phys. Rev. **121**, 630 (1961).
[28] R. Ching and C. Schaerf, Phys. Rev. **141**, 1320 (1966).
[29] T.-S. H. Lee, Few-Body Syst. Suppl. **6**, 526 (1992).
[30] E. DeSanctis *et al.*, *Proceedings of the 13th European Conference on Few Body Problems in Physics*, Elba, (World Scientific, Singapore, 1991); E. DeSanctis, A. B. Kaidalov, and L. A. Kondrachuk, Phys. Rev. C **42**, 1764 (1990).